

Joint time-variant spectral analysis — Part 2: A case study

Ramses G. Meza¹, Antonio Sierra², John P. Castagna³, and Umberto Barbato⁴

Abstract

The joint time-frequency and time-phase analysis applied to a field seismic data highlights lateral changes on preferential frequency and phase illumination at the target across secondary faults. Mutual thin-bed interference modeling suited for the case study area was performed using a well-tying well-based extracted wavelet assumed to be representative of the wavelet embedded on the input seismic data. The long coda of this wavelet is also present on the corresponding thin-bed waveform, indicating the possibility of more complex mutual interference patterns between thin beds and mutual interference at farther vertical separations between thin beds compared with what would occur for an embedded wavelet with a shorter coda. The observed lateral changes on preferential frequency and phase illumination on the seismic data are attributable to collocated lateral changes in the stacking patterns and variable occurrence of vertically adjacent thin beds, which are interpreted as lateral sediment deposition changes induced by the syndepositional activity of the secondary faults. This is a geologic scenario that had not been previously considered on the area until the evidence of this case study provide indirect support for it.

Introduction

A time-variant spectral analysis goal is to yield time-dependent amplitude data as a function of temporal frequency (Chakraborty and Okaya, 1995; Okaya, 1995; Partyka et al., 1999) and temporal phase (Castagna et al., 2016). Decomposing a seismic trace into time-variant magnitude-frequency and amplitude-phase spectra allows drawing inferences about discrete subsurface seismic events in terms of bed thickness, rock properties, and layering. The interpretation of time-frequency and time-phase analysis relies on the concept of preferential illumination (Castagna et al., 2003), which means that seismic events are preferentially illuminated by certain frequency and phase components, allowing making deductions about the subsurface otherwise not possible without spectrally decomposing the input data set.

The accompanying paper (Meza et al., 2018) presents examples of time-frequency and time-phase analysis performed on 1D synthetic traces generated out of binary-impedance earth models for target thin beds. These earth models first varied only in terms of the layered net-to-gross (NTG) ratio for a seismically isolated target bed. There was no observable change in terms of preferential frequency or phase illumination, although changes with NTG were observed on the amplitudes of the preferential spectral components. We then per-

formed another series of analysis using earth models consisting of a target thin-bed 100% NTG not seismically isolated. We observed that the most of the dramatic changes are observable on the preferential phase illumination, in which the canonical $\pm 90^\circ$ phase shift of a thin bed can be dramatically modified depending of the embedded wavelet and the stacking patterns of neighboring layers causing mutual interference with the target bed.

This paper is a case study that expands on the findings of Meza et al. (2016), by performing a joint time-frequency and time-phase analysis with interpretation criteria based on the mutual thin-bed interference effects described by Meza et al., (2018). Our goal is to present evidence that joint time-variant spectral analysis can provide compelling new insights into the process of building geologic frameworks out of 3D reflection seismic data.

Geologic framework, well-seismic ties, and thin-bed mutual interference assessment

Meza et al. (2016) present the initial results of a case study consisting of the application of phase decomposition (PD) time-phase analysis on a 3D seismic data set, corresponding to an undisclosed location in a geologic province where gas-bearing fluvial sandstones are known to yield elevated seismic amplitudes. Here, we

¹BHP Billiton Petroleum, Houston, Texas, USA. E-mail: ramses.meza@bhp.com.

²EOG Resources, Houston, Texas, USA. E-mail: antonio_sierra@eogresources.com.

³University of Houston, Houston, Texas, USA. E-mail: jcastagnaou@yahoo.com.

⁴Lumina Geophysical, Houston, Texas, USA. E-mail: umberto.barbato@luminageo.com.

Manuscript received by the Editor 15 February 2018; revised manuscript received 1 June 2018; published ahead of production 25 July 2018. This paper appears in *Interpretation*, Vol. 6, No. 4 (November 2018); p. 1–15, 21 FIGS.

<http://dx.doi.org/10.1190/INT-2018-0050.1>. © 2018 Society of Exploration Geophysicists and American Association of Petroleum Geologists. All rights reserved.

have extended the scope of observations and investigation from what Meza et al. (2016) report, by incorporating the analysis of thin-bed mutual interference effects on preferential spectral illumination, especially in time-phase analysis.

BHP Petroleum (BHP) is the operator of the licensed area. Seismic data we used consist of a far-angle stack, with angles of incidence ranging from 31° to 45° (central angle of incidence of the stack $\theta = 38^\circ$). This data set is a subset of a larger prestack depth migrated (PSDM) volume of recent acquisition and proprietary processing, which underwent a tilted-transverse isotropic Kirchhoff imaging workflow, aimed for improved structural mapping and higher amplitude fidelity for direct hydrocarbon indicator (DHI)-driven exploration and appraisal. This data set was converted to the two-way traveltime (TWT) domain using the vertical component of the interval velocity derived from PSDM velocity model building.

This volume was low-pass filtered as described by Meza et al. (2016). They observe that, for PD, the generated phase components are frequency dependent. This dependence is a consequence of the variation on layer thickness and interference between closely spaced events and can mislead the interpretation of PD results in case the layer under the scope is above seismic resolution. By removing certain ranges of higher frequencies from seismic data, layers originally above seismic resolution now become thin beds, therefore enhancing the discrimination potential of PD.

There is only one wellbore available in the area of interest. It contains modern logging measurements such as dipole sonic (P- and S-wave), density, neutron-porosity, gamma-ray, resistivity, and check shot. BHP performed the log QC and the subsequent petrophysical evaluation. This wellbore was tied to the seismic data by estimating a wavelet that, based on the reflectivity log, predicts most of the energy of the target signal, which in this case is the collocated seismic trace (White and Simm, 2003). This kind of algorithm allows obtaining wavelets with a nonconstant phase spectrum to achieve better well-seismic ties. Figure 1 shows the well-seismic tie using a Roy White (RW) wavelet based on the algorithm referenced above. The quality of the well-seismic tie is very good (70% synthetic-seismic correlation) based on the resemblance between the synthetic trace and the collocated far-angle seismic trace. The synthetic trace was generated using the density log, the check-shot corrected sonic log, and the S-wave log to generate an elastic-impedance (EI) log (Connolly, 1999). This was performed to obtain an angle-dependent impedance log that yields reflectivity contrasts that are more representative of the events within the nonzero angle stack ($\theta = 38^\circ$ in this case) to be tied. This is an improvement with respect of that of a 25 Hz zero-phase Ricker wavelet (0.64 synthetic-seismic correlation) well-tie performed, but now shown in this paper — for the whole vertical section of interest. The target event of interest is what Meza et al. (2016) refer to as event 1 (indicated with a black arrow in Figure 1), which is the shallowest on a stratigraphic sequence of gas-bearing thin-bedded sandstones. Event 1 is characterized by what seems to be a strong thin-bed response for what would be zero-phase seismic data. Its bed thickness is approximately 15 ms. A semiregional event is also indicated (the black-orange arrow) on the well-seismic tie in Figure 1, which spectral expression supported the first-order structural and stratigraphic interpretation later proposed in this case study.

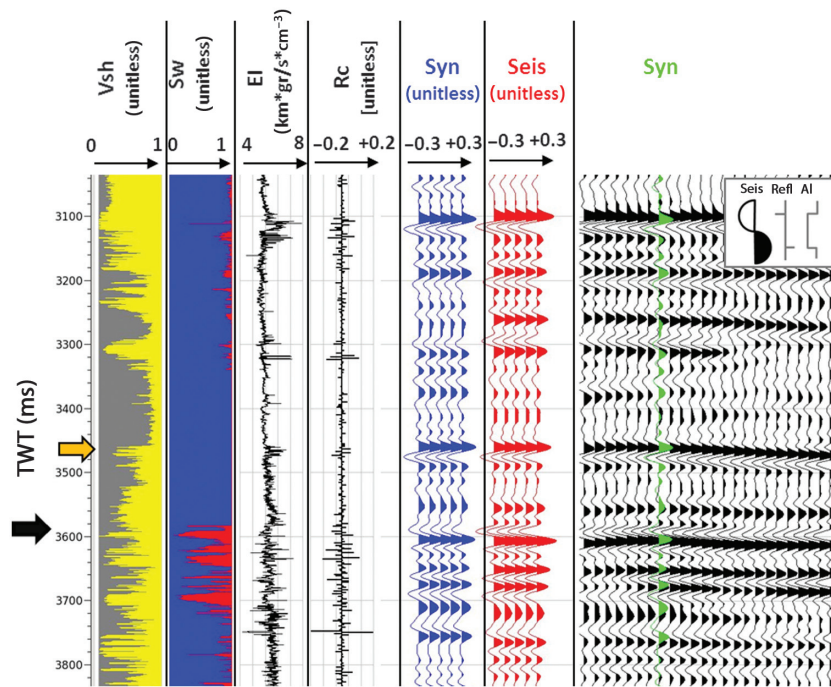


Figure 1. Well-seismic tie using an RW well-based extracted wavelet: (a) Vsh log, (b) Sw log, (c) EI ($\theta = 38^\circ$) log, (d) reflection coefficients for EI ($\theta = 38^\circ$), (e) synthetic trace, (f) collocated seismic trace, and (g) seismic section (black) with overlying synthetic trace (green). The top of event 1 is marked by the arrow and a shallower semiregional event with a black-orange arrow. Synthetic-seismic correlation coefficient = 0.70.

Figure 2a shows the time response of the RW wavelet, in which a long coda and some asymmetry of the wavelet around zero are observable. This wavelet can be differentiated to represent the corresponding scaled lower impedance thin-bed response (Widess, 1973) also shown in Figure 2a, in which the several sidelobes of the RW wavelet caused the thin-bed waveform to also have a long coda with more pronounced sidelobes, due to the wavelet differentiation. This thin-bed waveform seems to depart from a clear -90° waveform expected for a thin bed if a zero-phase embedded seismic wavelet is assumed. The autocorrelation of the corresponding lower impedance thin-bed waveform, as shown in Figure 2b,

depicts several nonzero lags in which constructive and destructive mutual interference of thin beds can occur. The main consequence of the wavelet having a long coda is to have a far-reaching interference effects at longer ver-

tical separations (lags) as compared with a more compact wavelet.

In a similar fashion as performed in [Meza et al., \(2018\)](#), we have also modeled the mutual interference

of identical lower impedance thin beds with centers separated by some nonzero lags to observe how these interference patterns affect the time-frequency and time-phase analysis, as shown in [Figures 3, 4, 5, 6, 7, 8, and 9](#). The reference thin-bed center is located at 150 ms, and its seismically isolated response is represented in [Figure 3](#), reaching preferential phase illumination closer to 0° rather than -90° . As shown in [Figures 4–9](#), as the two thin-bed waveforms become closer to each other — even at far distances — there are some time-phase changes in the vicinity of the reference layer without a strong change in its own preferential illumination, and then the composite waveform starts undergoing significant changes that become evident as major changes of the phase components that preferentially illuminate the reference thin bed, in a pattern with no clear consistency. In terms of time-frequency analysis, there is no resolvable change in the

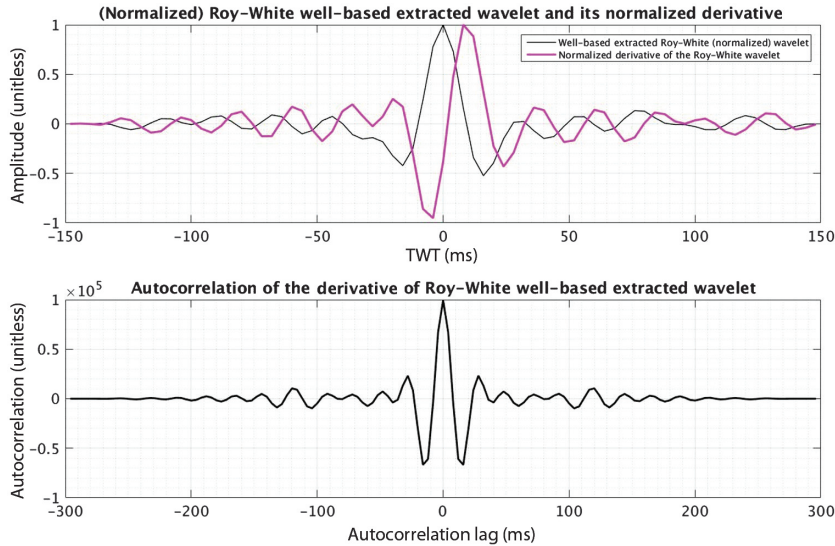


Figure 2. (a) The RW well-based extracted wavelet (the black) and the corresponding normalized lower impedance thin-bed waveform (magenta). (b) Autocorrelation of a lower impedance thin-bed waveform based on the RW well-based extracted wavelet on (a).

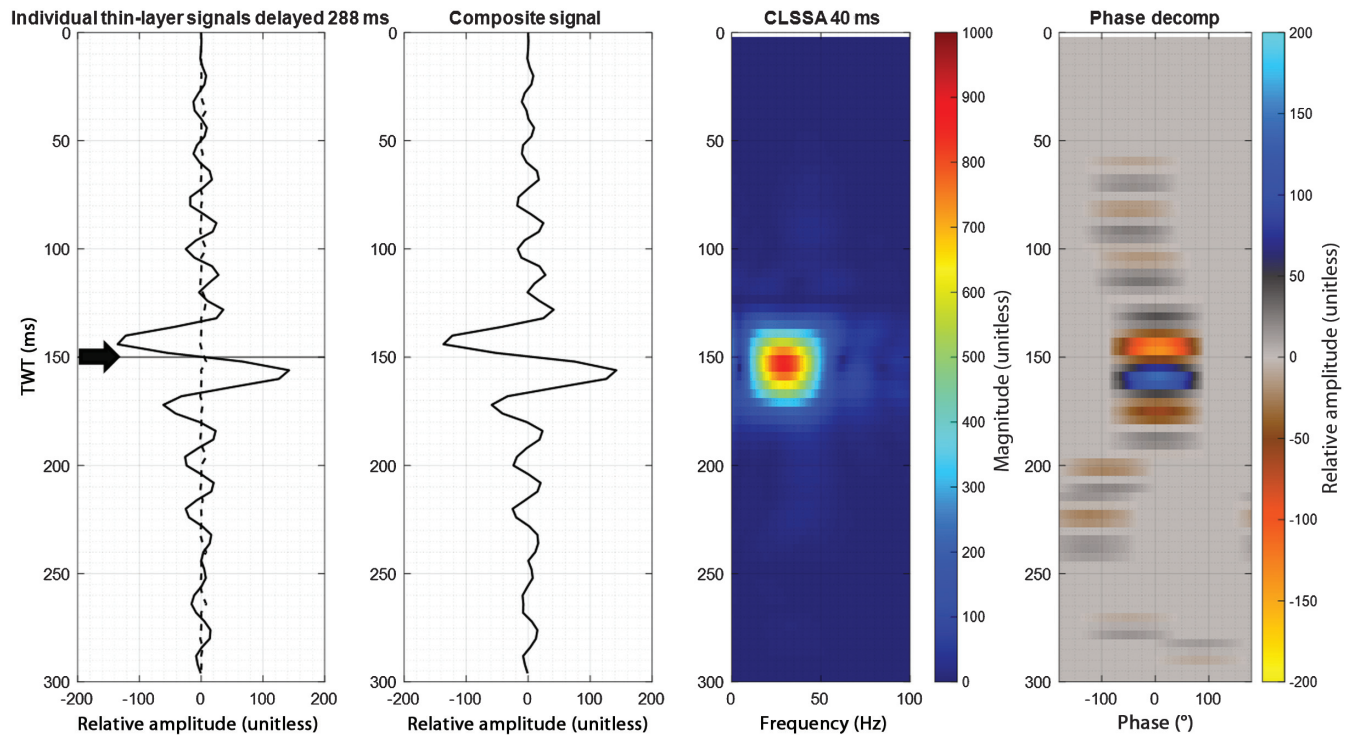


Figure 3. Time-variant spectral responses of the combination of two mutually interfering thin-bed waveforms with their centers (highlighted with arrows) separated by 288 ms, based on an RW well-based extracted wavelet. (a) Reference (targeted) thin-bed waveform (the solid line) and interfering thin-bed waveform (the dashed line), (b) composite seismic response of the waveforms shown in (a), (c) CLSSA time-frequency analysis of the composite seismic response, and (d) PD time-phase analysis of the composite seismic response.

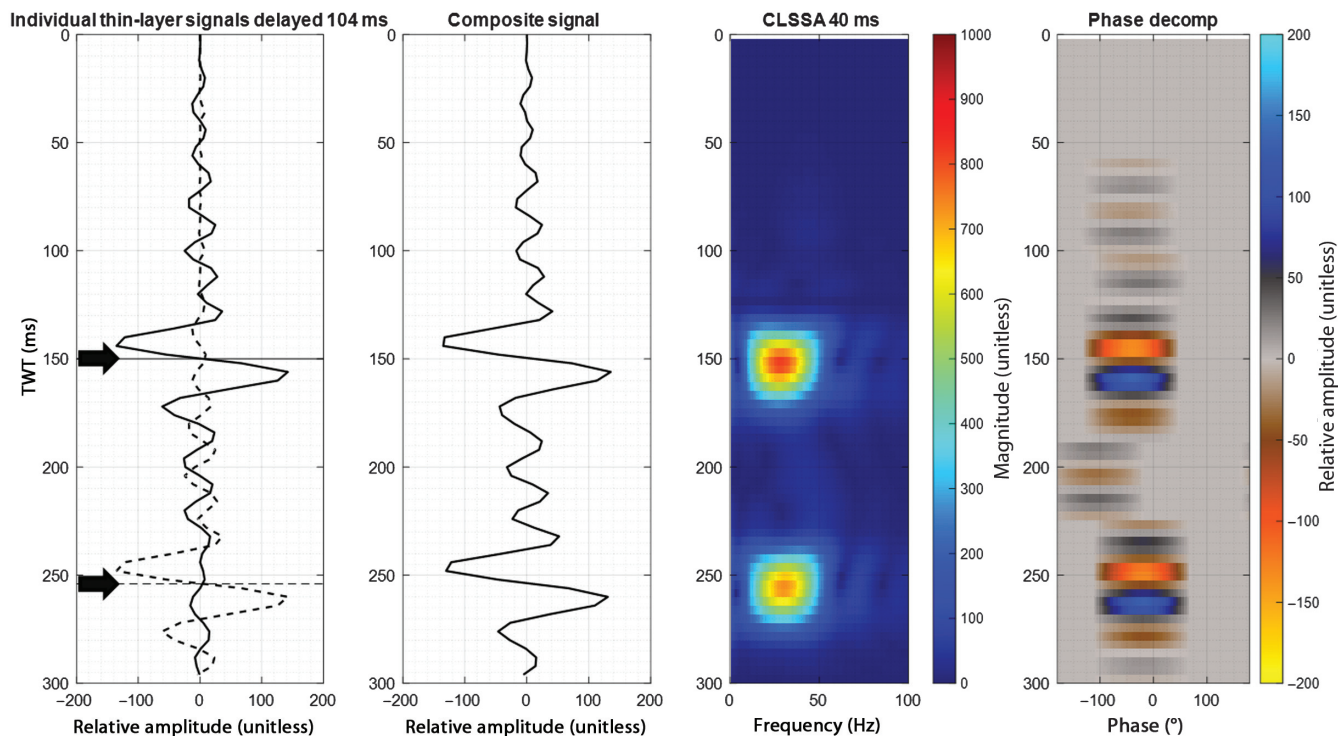


Figure 4. Time-variant spectral responses of the combination of two mutually interfering thin-bed waveforms with their centers (highlighted with arrows) separated by 104 ms, based on an RW well-based extracted wavelet. (a) Reference (targeted) thin-bed waveform (the solid line) and interfering thin-bed waveform (the dashed line), (b) composite seismic response of the waveforms shown in (a), (c) CLSSA time-frequency analysis of the composite seismic response, and (d) PD time-phase analysis of the composite seismic response.

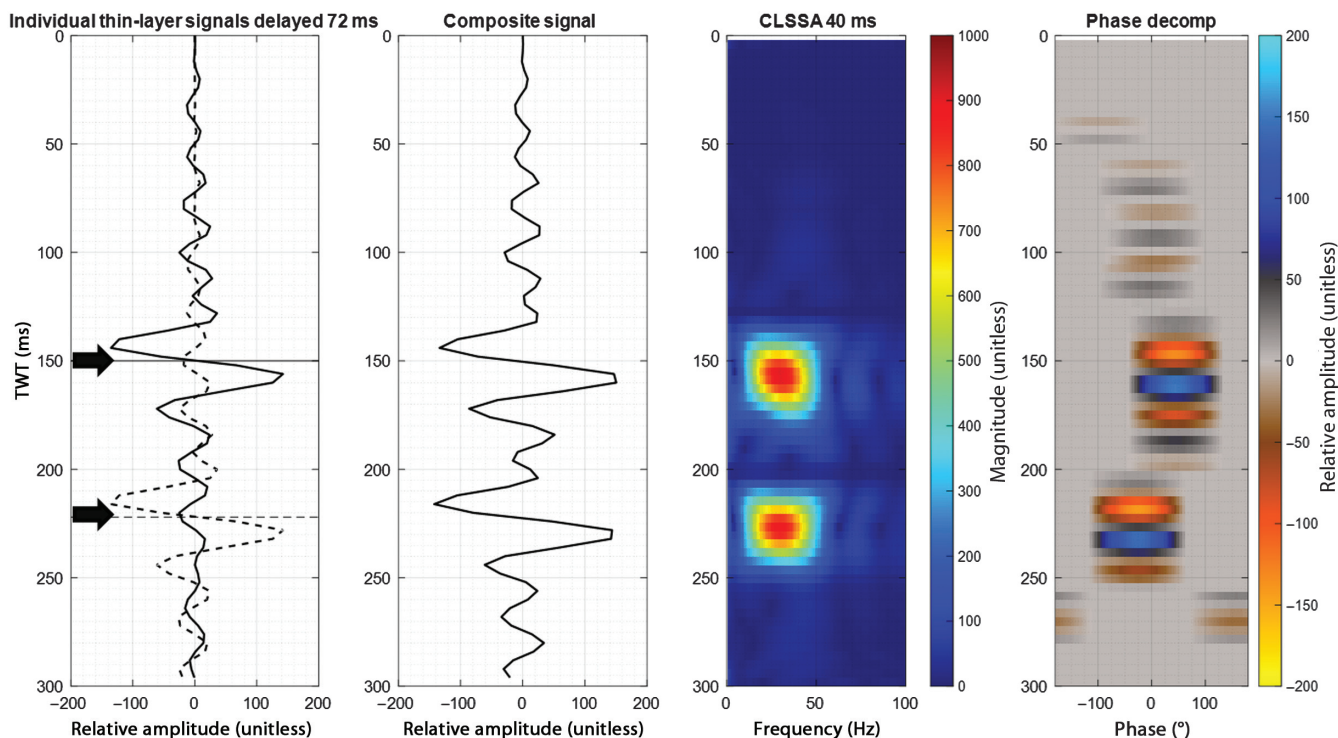


Figure 5. Time-variant spectral responses of the combination of two mutually interfering thin-bed waveforms with their centers (highlighted with arrows) separated by 72 ms, based on an RW well-based extracted wavelet. (a) Reference (targeted) thin-bed waveform (the solid line) and interfering thin-bed waveform (the dashed line), (b) composite seismic response of the waveforms shown in (a), (c) CLSSA time-frequency analysis of the composite seismic response, and (d) PD time-phase analysis of the composite seismic response.

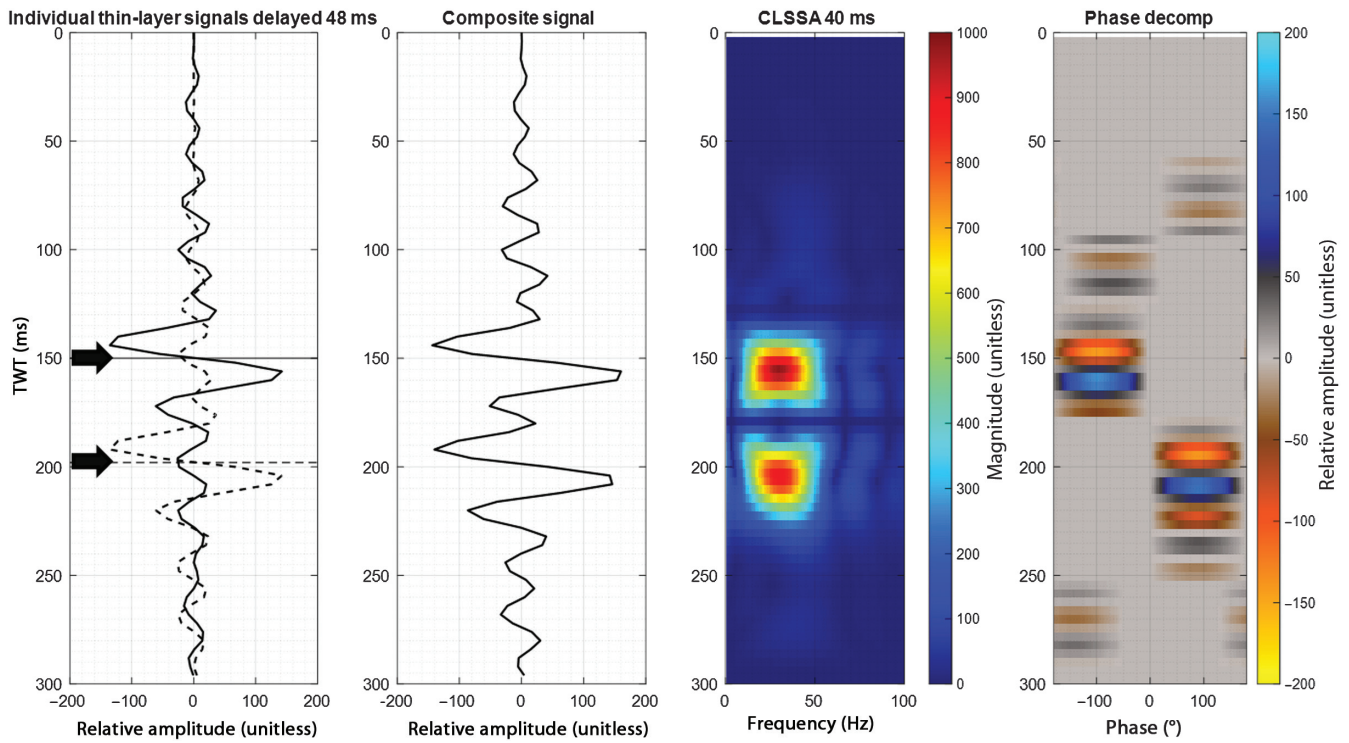


Figure 6. Time-variant spectral responses of the combination of two mutually interfering thin-bed waveforms with their centers (highlighted with arrows) separated by 48 ms, based on an RW well-based extracted wavelet. (a) Reference (targeted) thin-bed waveform (the solid line) and interfering thin-bed waveform (the dashed line), (b) composite seismic response of the waveforms shown in (a), (c) CLSSA time-frequency analysis of the composite seismic response, and (d) PD time-phase analysis of the composite seismic response.

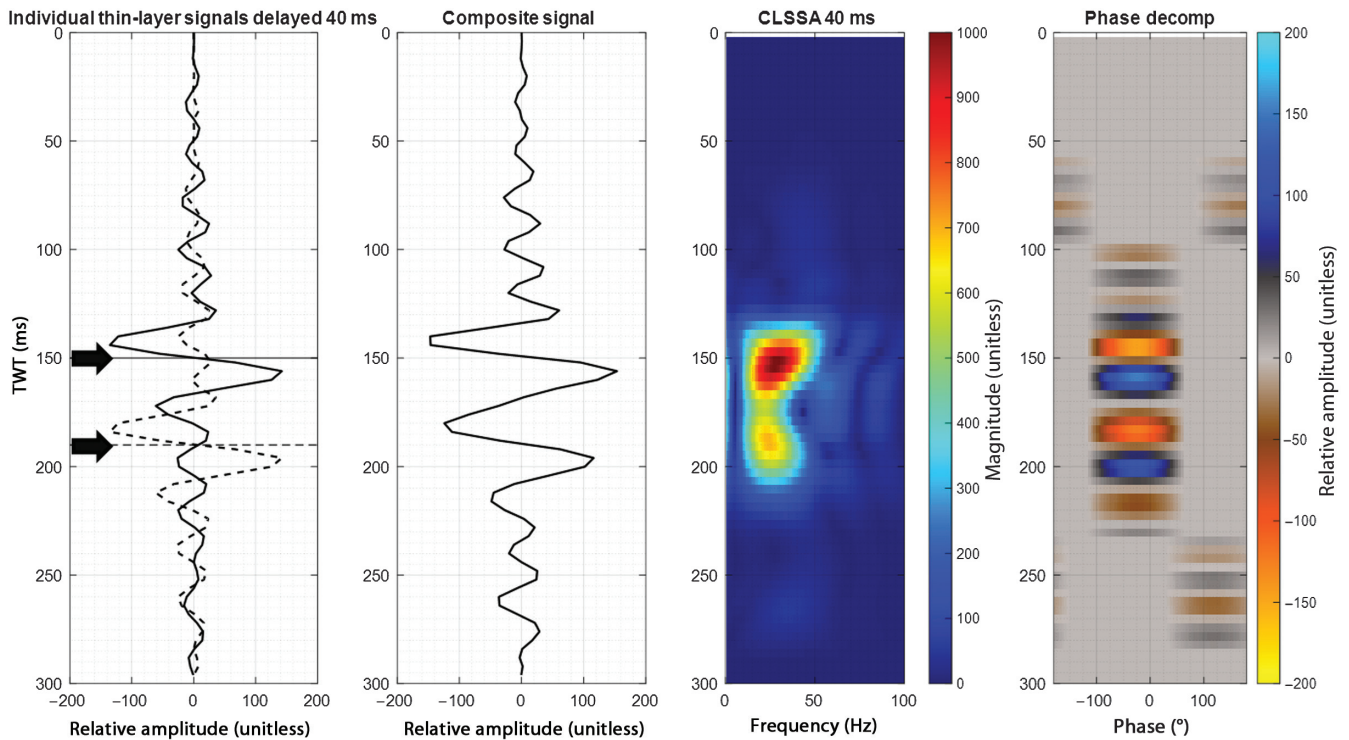


Figure 7. Time-variant spectral responses of the combination of two mutually interfering thin-bed waveforms with their centers (highlighted with arrows) separated by 40 ms, based on an RW well-based extracted wavelet. (a) Reference (targeted) thin-bed waveform (the solid line) and interfering thin-bed waveform (the dashed line), (b) composite seismic response of the waveforms shown in (a), (c) CLSSA time-frequency analysis of the composite seismic response, and (d) PD time-phase analysis of the composite seismic response.

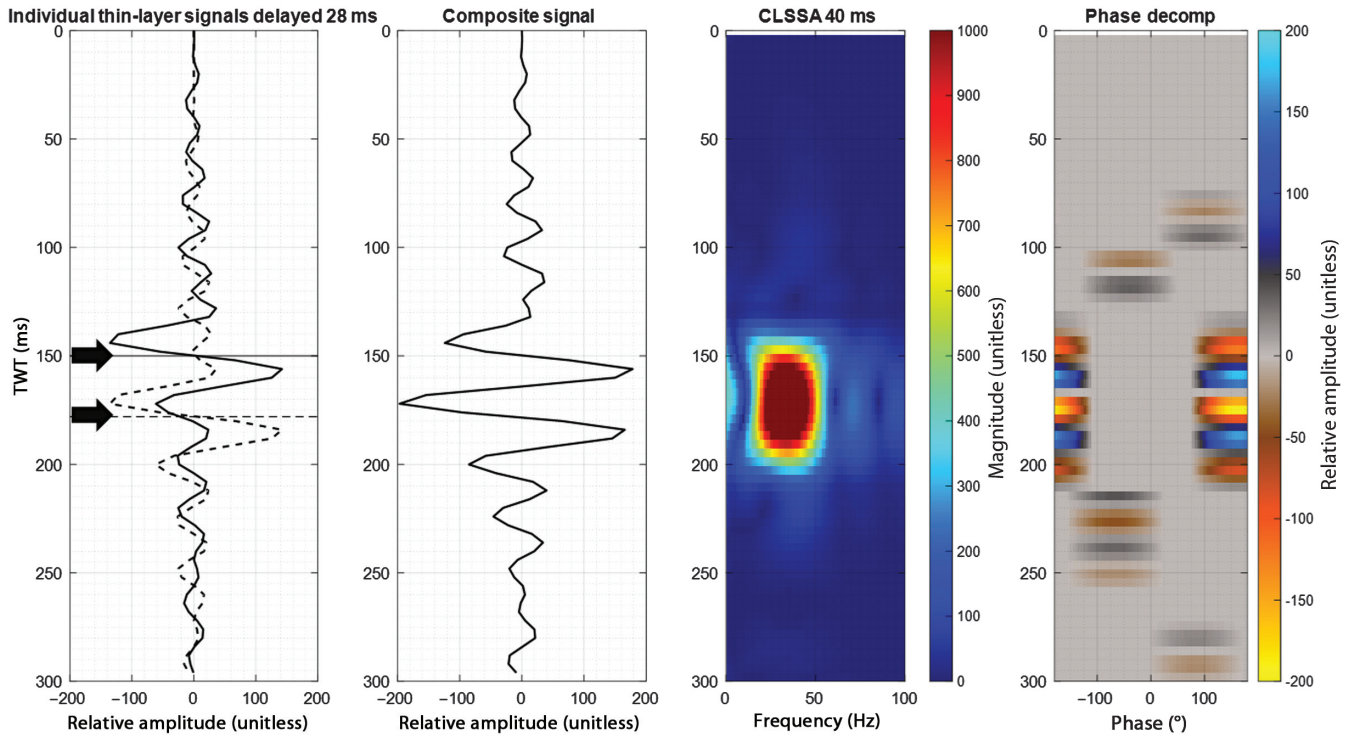


Figure 8. Time-variant spectral responses of the combination of two mutually interfering thin-bed waveforms with their centers (highlighted with arrows) separated by 28 ms, based on an RW well-based extracted wavelet. (a) Reference (targeted) thin-bed waveform (the solid line) and interfering thin-bed waveform (the dashed line), (b) composite seismic response of the waveforms shown in (a), (c) CLSSA time-frequency analysis of the composite seismic response, and (d) PD time-phase analysis of the composite seismic response.

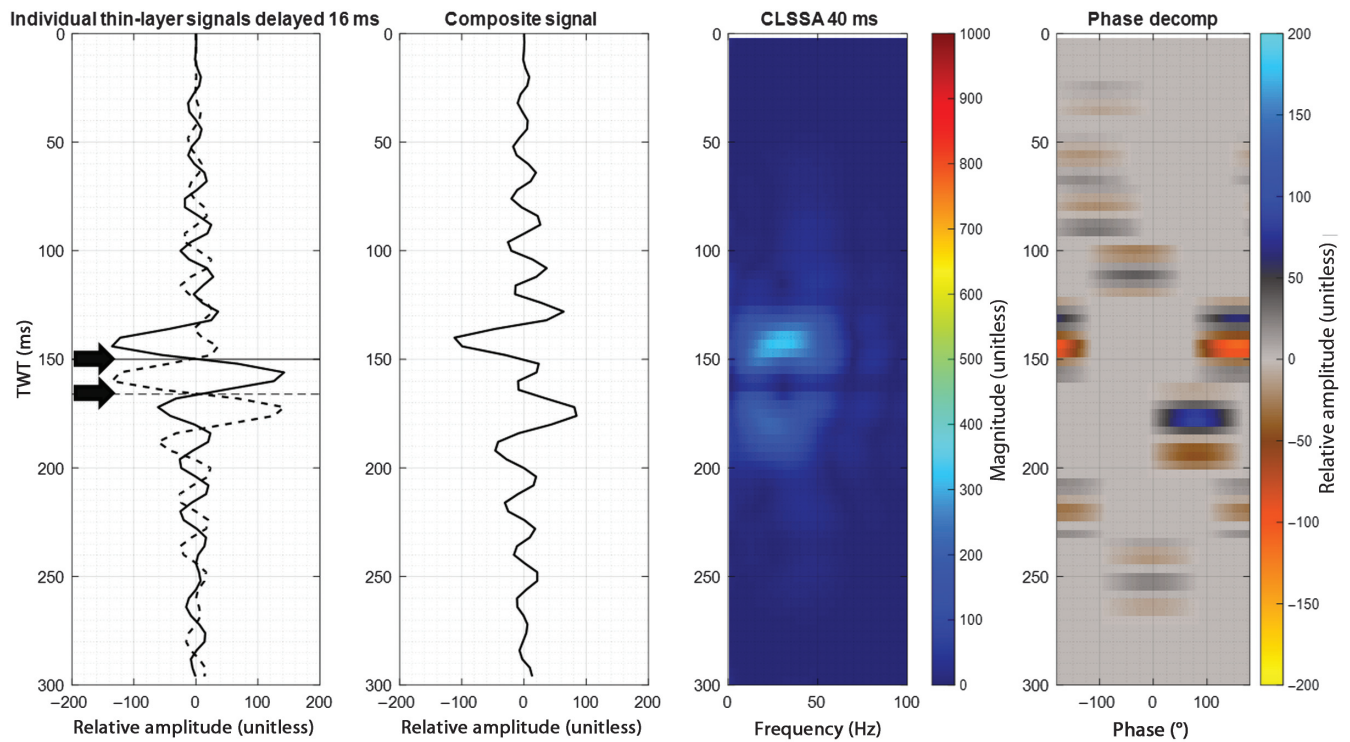


Figure 9. Time-variant spectral responses of the combination of two mutually interfering thin-bed waveforms with their centers (highlighted with arrows) separated by 16 ms, based on an RW well-based extracted wavelet. (a) Reference (targeted) thin-bed waveform (the solid line) and interfering thin-bed waveform (the dashed line), (b) composite seismic response of the waveforms shown in (a), (c) CLSSA time-frequency analysis of the composite seismic response, and (d) PD time-phase analysis of the composite seismic response.

preferential frequency illumination, with changes on the peak magnitude that seem to be at first not easily defined by any pattern.

The comparison of the two well-tying wavelets, in the temporal and spectral domains, is shown in Figure 10. The spectral response was obtained using

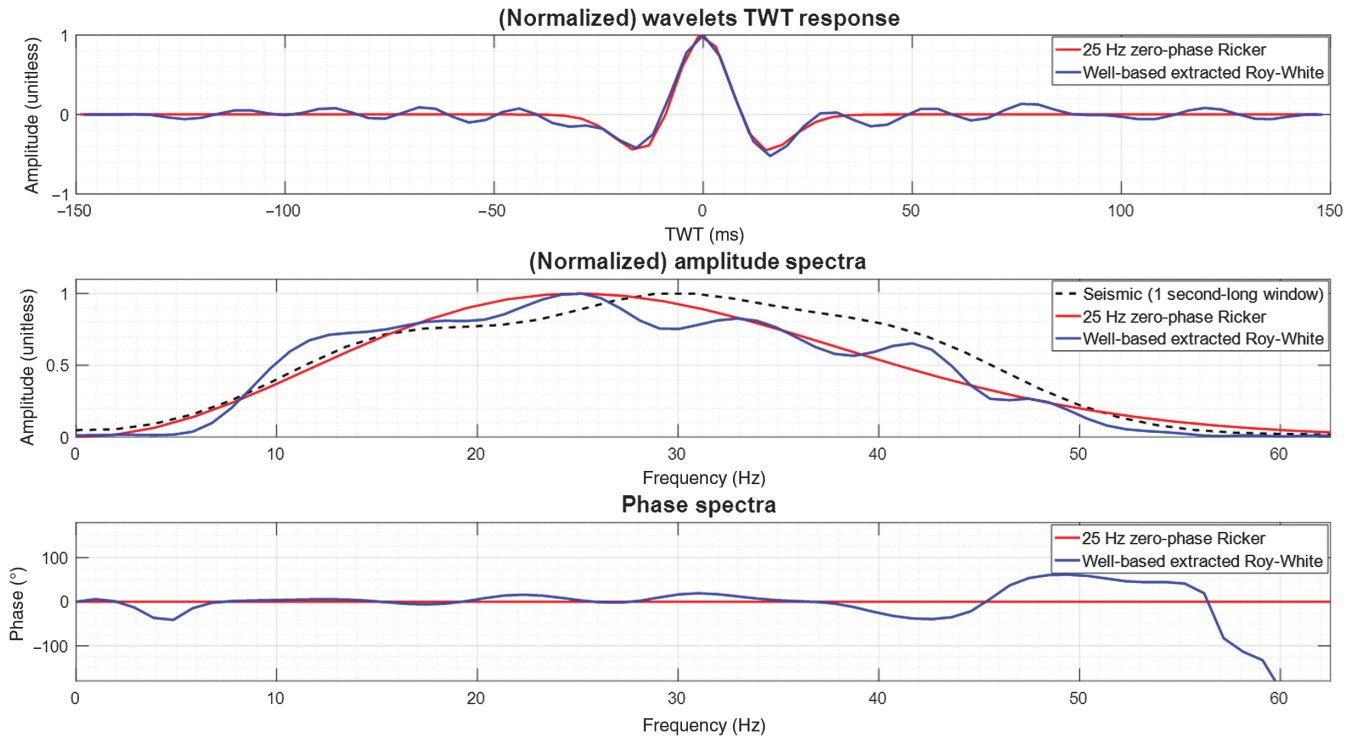


Figure 10. Comparison of a 25 Hz zero-phase Ricker (red) and well-based extracted RW (the blue) wavelets. (a) Temporal domain, (b) normalized amplitude spectra (seismic amplitude spectrum in the black dashed line), and (c) phase spectra.

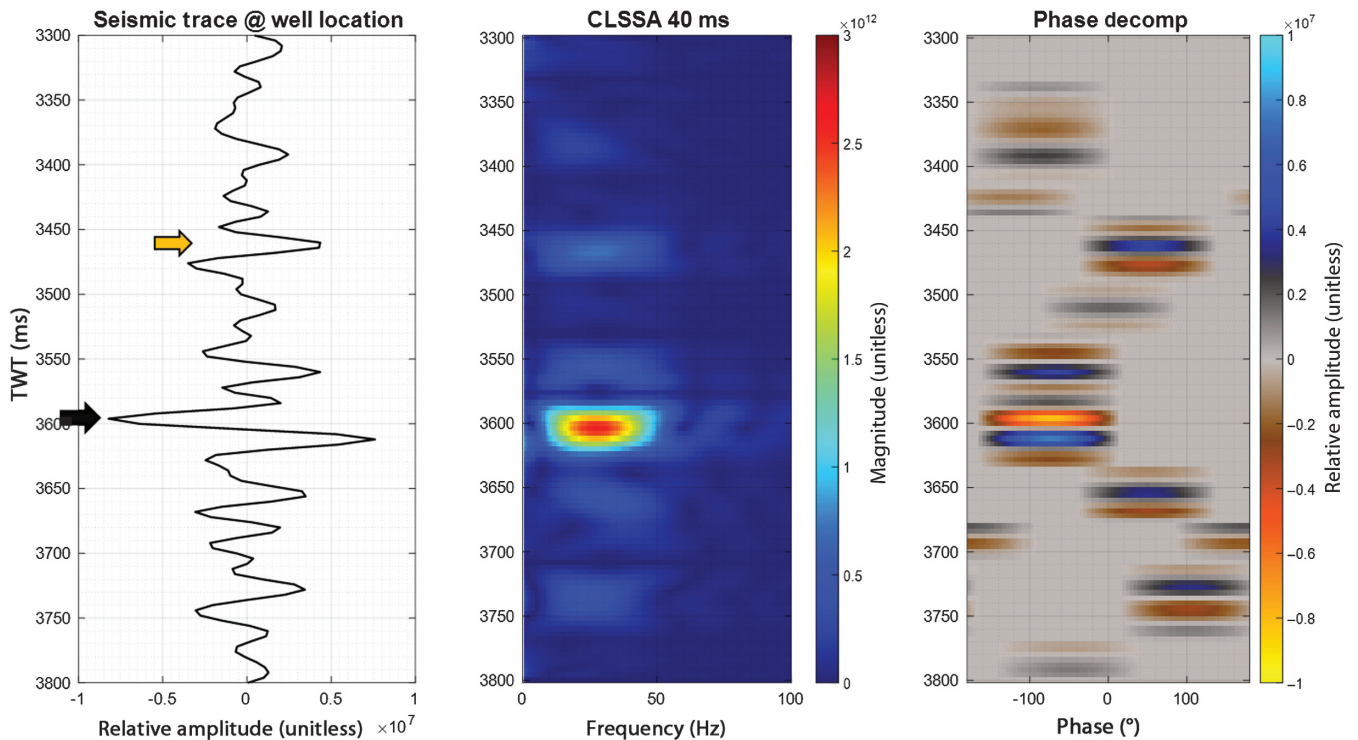


Figure 11. Time-variant spectral responses of a seismic trace at the wellbore location: (a) wellbore-located seismic trace for the formation of interest (top of the main target marked with the black arrow and the shallower semiregional event indicated with the black-orange arrow), (b) CLSSA time-frequency analysis, and (c) PD time-phase analysis.

the fast-Fourier transform (FFT) in its classic time-invariant form. The two wavelets largely resemble each other in the temporal domain (Figure 10a), in terms of the character of their main peaks and main sidelobes, but largely differ in their codas. The RW wavelet has several sidelobes that are the cause for the complex interference patterns between two thin beds when this wavelet is assumed to be representative of the composite seismic response. By comparing the wavelets in terms of their amplitude spectra (Figure 10b), the RW spectrum is not as smooth as that of the 25 Hz Ricker wavelet and that of the actual seismic data, the latter obtained via FFT over a 1 s long window including the target interval. Even though both wavelet bandwidths are very comparable, the RW spectral roughness, combined with its nonconstant phase spectra (Figure 10c), yield the long coda observed on the temporal response. Although the RW wavelet phase spectra averages close to zero phase within most of the signal bandwidth, such phase departures from mean zero phase at each frequency will have a different impact on the temporal response based on the Fourier transform shift theorem (Bracewell, 2000).

Joint time-variant spectral analysis to 3D surface reflection seismic data set

Time frequency using a 40 ms window constrained least-squares spectral analysis or CLSSA (Purveyar et al., 2012) and time phase using PD (Castagna et al., 2016) analyses were performed on the 3D seismic volume over the area of interest. Figure 11 depicts a seismic trace at the wellbore location (Figure 11a) over a time span to show the formation of interest, with the seismic top of the event of interest marked with a black arrow. The corresponding frequency and phase gathers are displayed in Figure 11b and 11c, respectively. On the frequency gather, the event clearly dominates the magnitude response with good temporal and frequency localization. Most of the events display similar preferential frequency illumination at approximately 25–30 Hz.

On the other hand, amplitudes of events as seen on the phase gathers are more comparable, and, more importantly, events on the input seismic trace are preferentially illuminated at significantly different phase components. The target event is preferentially illuminated closer to the -90° or PD odd component. This observation disagrees with the modeled thin-bed mutual interference analysis for an isolated waveform

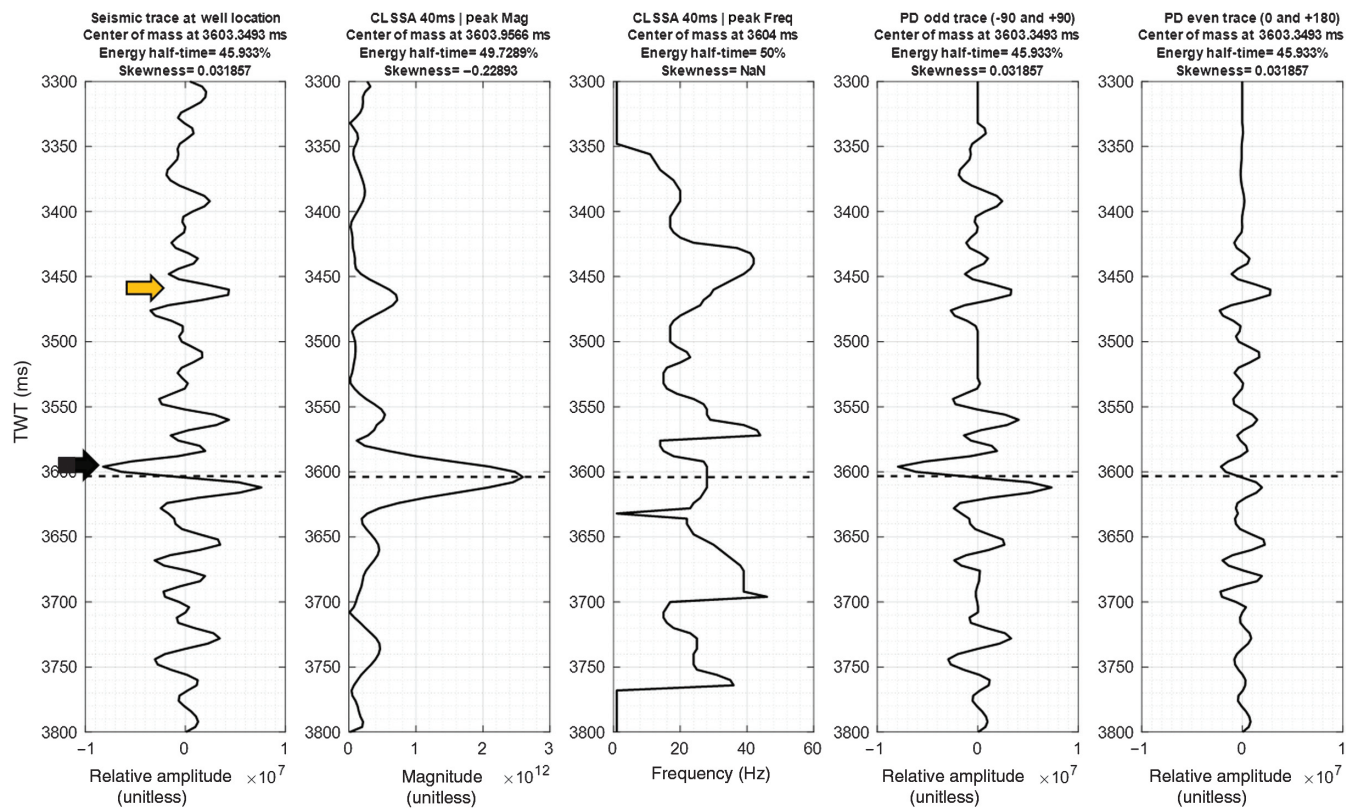


Figure 12. Time-variant spectral analysis attributes of a seismic trace at the wellbore location: (a) wellbore-located seismic trace for the formation of interest (top of the main target marked with the black arrow and the shallower semiregional event indicated with the black-orange arrow), (b) CLSSA peak magnitude, (c) CLSSA peak frequency (Hz), (d) PD odd trace (-90° and $+90^\circ$), and (e) PD even trace (0° and 180°). On top of each track, there is the corresponding center of mass location, energy half-time, and skewness. Interval for metric calculation for all tracks is defined by the interpreted top and base events on the seismic trace on (a). Center of mass for each track is shown as a dashed line.

considering the RW wavelet that ties the wellbore. In addition, there are several thin beds in close proximity to the target event as observed on the synthetic seismogram, adding complexity to the interference patterns that ultimately affect the preferential phase illumination at the target.

Certain key attributes or subsets were obtained from the frequency and phase gathers to reduce the data dimensionality of the time-variant spectral analyses for ease of interpretation in a 3D context. Figure 12a shows the same wellbore-located seismic trace along with some attributes such as time-frequency peak magnitude (Figure 12b), time-frequency peak frequency (Figure 12c), time-phase composite odd trace (Figure 12d), and time-phase composite even trace (Figure 12e). Just for completeness, center of mass metrics was also calculated for all attributes on this display (Barnes, 2016; Meza et al., 2018), depicting no clear indication of difference of energy distribution vertically within the thin bed. In terms of time-frequency analysis, the event of interest (indicated with a black arrow) yields optimal illumination via peak magnitude, whereas its peak frequency is approximately 25–30 Hz. In the case of time-phase analysis, the main event exhibits preferential

illumination at this location by using phase components closer to the odd rather than the even component. For comparison, the shallower semiregional event in Figure 12a (indicated with a black-orange arrow) seems to be close to a $+90^\circ$ waveform, which indeed is also better illuminated by the odd component.

Horizon-based attribute extractions using a 20 ms long horizon-centered window were performed to highlight lateral variations of the attributes for the same target event, as shown in Figure 13. The structural style of this province is dominated by what is interpreted as postdepositional extensional faulting that produced tilted blocks (horsts and grabens) that define the geometry of the hydrocarbon traps. Figure 13a shows the TWT structural map at the top of the target event, depicting a very well-defined map-view expression of the major horst targeted by the wellbore. It is of the utmost importance to emphasize that major horst and grabens identified on seismic are also compartmentalized and/or segmented by minor or secondary extensional faults, giving rise to smaller horsts and grabens. The elevated amplitude anomaly on the input data is shown in Figure 13d, which extends to most of the major horst. The map-view footprint of this anomaly is nearly replicated

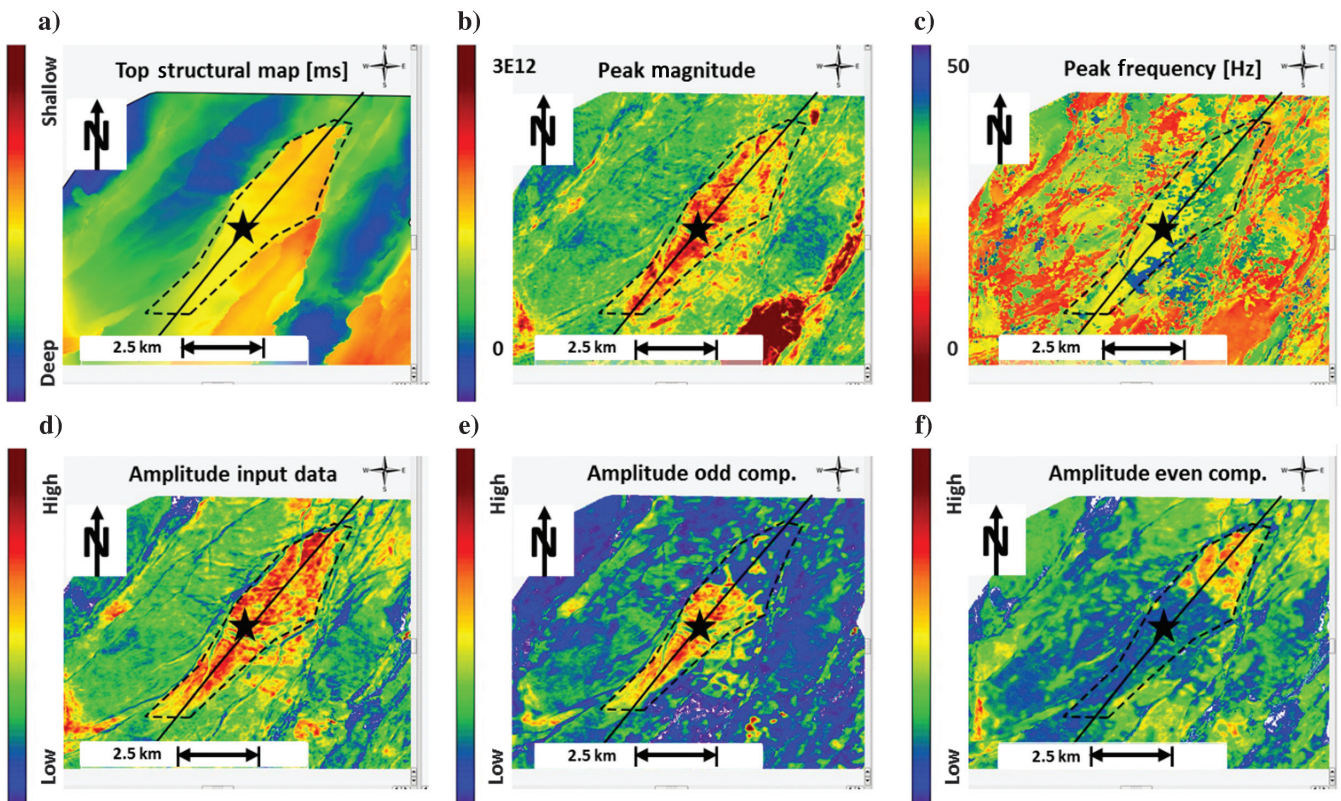


Figure 13. Horizon-based attribute extractions along the target event using a 20 ms long horizon-centered window: (a) TWT structural map, (b) median CLSSA peak magnitude, (c) median CLSSA peak frequency, (d) maximum-negative amplitude of input data, (e) maximum-negative amplitude of the PD odd component, and (f) maximum-negative amplitude of the PD even component. The wellbore location is indicated by a black star. The potential field extent based on conventional amplitude analysis is outlined with the dashed-line polygon. An arbitrary line (Figure 14) is indicated by the southwest–northeast black line. Absolute geographic location cannot be displayed due to the proprietary data used. All displayed quantities other than peak frequency are normalized and relative.

by the CLSSA peak magnitude map in Figure 13b, and to a lesser degree by CLSSA peak frequency in Figure 13c. Both attributes exhibit less continuity and weaker

strength of the anomaly toward the northeast, as compared with the input data amplitude shown in Figure 13d. Variations of peak magnitude within the anomaly south-

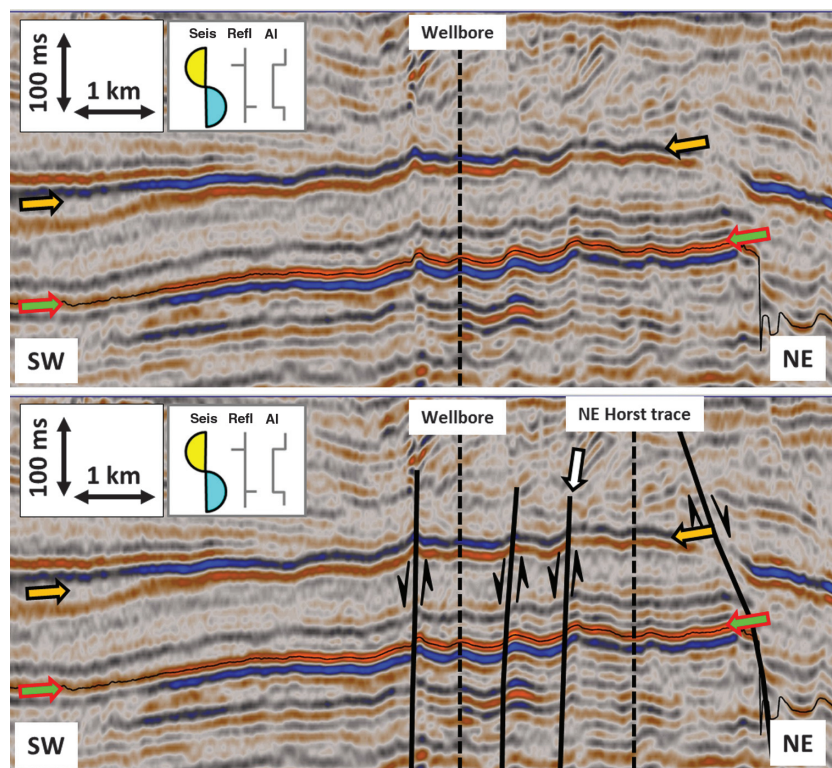


Figure 14. Southwest–northeast vertical section displaying the input seismic data (a) without and (b) with overlaid fault interpretation. The target horizon top event is indicated with the green-red arrow and tracked by the black horizon, and the shallower semiregional event is indicated with the black-orange arrow. The northwest–southeast fault under scope is indicated with a black-white arrow, whereas the wellbore-collocated and sample northeast horst sample traces are also indicated with the black dashed lines. The line orientation is indicated in Figure 13. The polarity is such that the red amplitudes represent soft events.

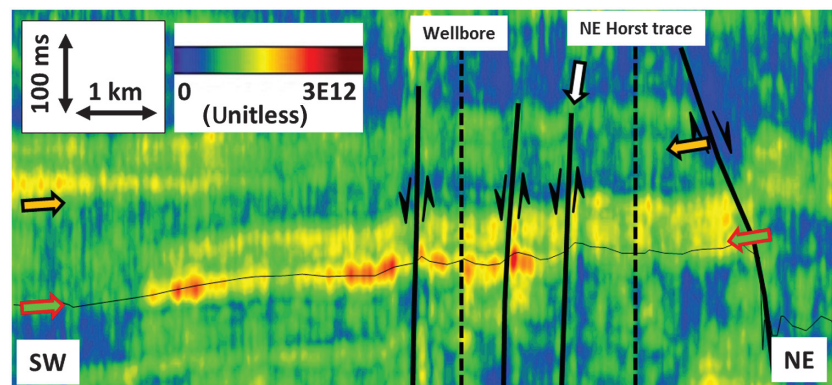


Figure 15. Southwest–northeast vertical section displaying the CLSSA peak magnitude with overlaid fault interpretation. The target horizon top event is indicated with the green-red arrow and tracked by the black horizon, and the shallower semiregional event is indicated with the black-orange arrow. The northwest–southeast fault under scope is indicated with a black-white arrow, whereas the wellbore-collocated and sample northeast horst sample traces are also indicated with the black dashed lines. The line orientation is indicated in Figure 13.

west segment are mostly associated with relatively constant lower peak frequencies, whereas weaker peak magnitude variations in the northeast segment are mostly correlated with relatively higher and nearly uniform peak frequencies. For each separate segment, peak magnitude variations are expected to be mainly due to changes in the contrasts in background-reservoir interface properties, rather than bed thickness or tuning because the peak frequency is nearly constant for each segment of the two segments of the anomaly.

As shown by Meza et al. (2016), in this area the most outstanding observation occurs when analyzing the anomaly using PD. The amplitude anomaly as seen on the input data is sharply dissected in the northwest–southeast direction, tending to be preferentially illuminated by the odd component on the southwest segment (Figure 13e) and by the even component on the northeast segment (Figure 13f). The northwest–southeast sharp change in preferential illumination closely tracks the trace of an intersecting secondary extensional fault with a northwest–southeast strike: Complex faulting patterns occur in the province due to the presence of several fault set directions that create hexagonal faulting patterns. This minor faulting is more evident on the vertical seismic section shown in Figure 14a and 14b, with and without overlaid fault interpretation, respectively, on the input seismic data set. The northwest–southeast-striking fault corresponding to the sharp change mentioned earlier (Figure 13e and 13f) is indicated in Figure 14b and onward with a black-white arrow. Based only on the input data set, there is no conclusive observation about any sudden lateral change of seismic character at the target (indicated with the red-green arrows) across any of the secondary faults. Also, the shallower semiregional event mentioned earlier (Figure 12) is indicated with a black-orange arrow. To compare spectral responses across the secondary fault, we selected a sample trace located on the northeast horst, which is indicated in Figure 14b and onward.

Figures 15, 16, 17, and 18 display CLSSA peak magnitude, CLSSA peak fre-

quency, PD odd, and PD even attributes, respectively, for the same southwest–northeast vertical section. There is some indication of attribute change across a secondary fault, which exhibits higher but somewhat discontinuous peak amplitude (Figure 15) on the southwest portion of the trap, compared with its northeast portion. In the case of peak frequency (Figure 16), the target tends to exhibit lower peak frequency toward the southwest portion of the trap compared with the rest. Because two or more thin beds sharing the same temporal thickness will tune at the same peak frequency (Partyka et al., 1999) regardless of their relative differences on their elastic properties, then any difference on peak magnitude for the same peak frequency is assumed to be independent of tuning but dependent on the relative difference between the elastic properties of the layers. Based on this premise, we interpret the higher peak magnitudes with lower peak frequencies in the southwest portion of the target as unlikely to be the consequence of tuning effects, which would require higher peak frequencies collocated with the observed peak magnitudes.

The sharp dissection of the anomaly observed on the map views in Figure 13e and 13f is confirmed on the corresponding vertical sections in Figures 17 and 18. The PD odd component preferentially illuminates the target event for most of the length of the section until a secondary extensional fault is reached, and then the preferential illumination of the event is switched to the PD even component. This observation is reinforced by the time-frequency and time-phase spectral analyses of a sample trace on the footwall or northeast horst of the secondary fault, shown in Figure 19, and the spectral attribute traces shown in Figure 20. The target event exhibits weaker time-frequency magnitudes and preferential illumination on the even component, which has significantly increased with respect to the illumination of the odd component, in closer agreement to the modeled mutual interference analysis for an isolated thin-bed waveform when the well-tying RW wavelet is taken as representative of the seismic data set.

Discussion

We interpret these observations to be supportive evidence of the syndepositional character of the particular secondary fault around the geologic time of deposition of the target bed. Although no growth interval can be seismically identified at the hanging wall of the secondary fault due to the subresolution vertical fault offset, indirect evidence

of such a growth interval can be the stronger peak magnitude collocated with lower peak frequencies that might be associated with thicker stratal bedsets comprising the target bed and its underlying beds. Weaker seismic events underneath the target bed at the footwall, compared with correlated events on the hanging wall, can support the hypothesis that fewer and weaker events can be a consequence of fewer reflectivity contrasts underneath the target, signifying larger sand scarcity on the footwall compared with the hanging wall. These differences in stratal bedsets underlying the target can yield different thin-bed interference patterns that can dramatically affect the preferential phase illumination of the target bed, even if the target bed itself does not significantly change across the fault, as shown previously by the modeling of thin-bed mutual interference.

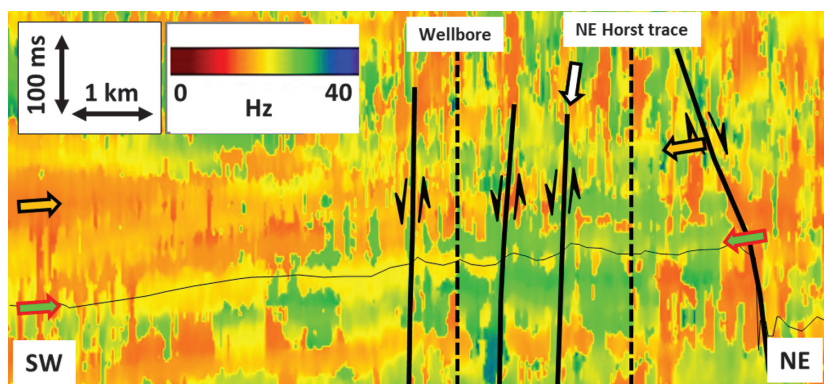


Figure 16. Southwest–northeast vertical section displaying the CLSSA peak frequency with overlaid fault interpretation. The target horizon top event is indicated with the green-red arrow and tracked by the black horizon, and the shallower semiregional event is indicated with the black-orange arrow. The northwest–southeast fault under scope is indicated with a black-white arrow, whereas the wellbore-collocated and sample northeast horst sample traces are also indicated with the black dashed lines. The line orientation is indicated in Figure 13.

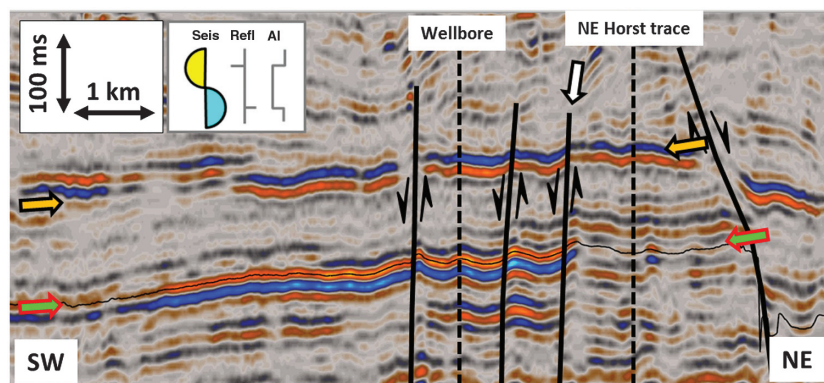


Figure 17. Southwest–northeast vertical section displaying the PD odd component with overlaid fault interpretation. The target horizon top event is indicated with the green-red arrow and tracked by the black horizon, and the shallower semiregional event is indicated with the black-orange arrow. The northwest–southeast fault under scope is indicated with a black-white arrow, whereas the wellbore-collocated and sample northeast horst sample traces are also indicated with the black dashed lines. The line orientation is indicated in Figure 13.

During geologic times before the deposition of the target layer, this secondary fault might have been syndepositional and then the fault significantly reduced or stopped its displacement before or around the time of deposition of the target bed. The semiregional shallower event seen on the input seismic data set (Figure 14) approximately 120 ms shallower than the target bed is also displaced by the same secondary fault, but we claim that the fault character at this later geologic time is post-

depositional. This interpretation is supported by the fact that this semiregional event, as seen on the input data, is very close to an isolated $+90^\circ$ waveform, which does not exhibit the changes across faults that the target bed does, especially considering that it is mostly preferentially illuminated by the PD odd component on both blocks of the secondary fault.

This conceptual interpretation is a first-order geologic scenario shown in the vertical section in Figure 21.

The syndepositional character of the secondary fault for the target bed formation is schematically represented as sudden lateral changes in the formation sandstones thickness, continuity, and abundance from one bounding block of the secondary fault to the other. The impact of this concept on exploration can be significant, for instance, sand scarcity within the formation on the northeast horst can make it less attractive as a drilling target due to smaller gross rock volumes. However, this can also make the hanging wall of the secondary fault more attractive because more sand scarcity on its footwall can lead to a lower chance of sand juxtaposition along the secondary fault, reducing the risk related to the integrity of the trap edge of the southwest segment of the overall trap.

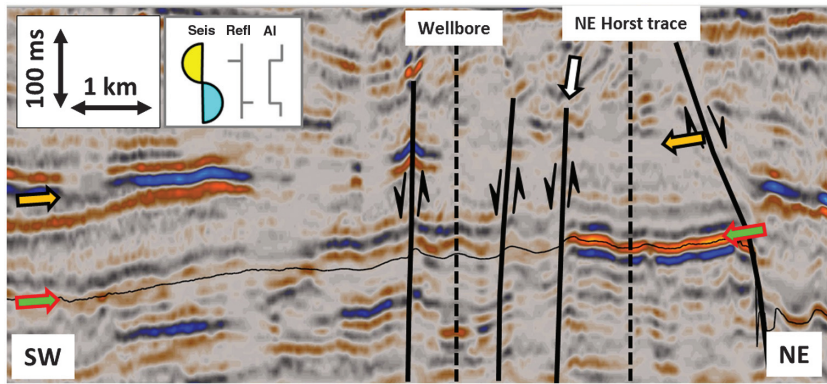


Figure 18. Southwest–northeast vertical section displaying the PD even component with overlaid fault interpretation. The target horizon top event is indicated with the green-red arrow and tracked by the black horizon, and the shallower semiregional event is indicated with the black-orange arrow. The northwest–southeast fault under scope is indicated with a black-white arrow, whereas the wellbore-collocated and sample northeast Horst sample traces are also indicated with the black dashed lines. The line orientation is indicated in Figure 13.

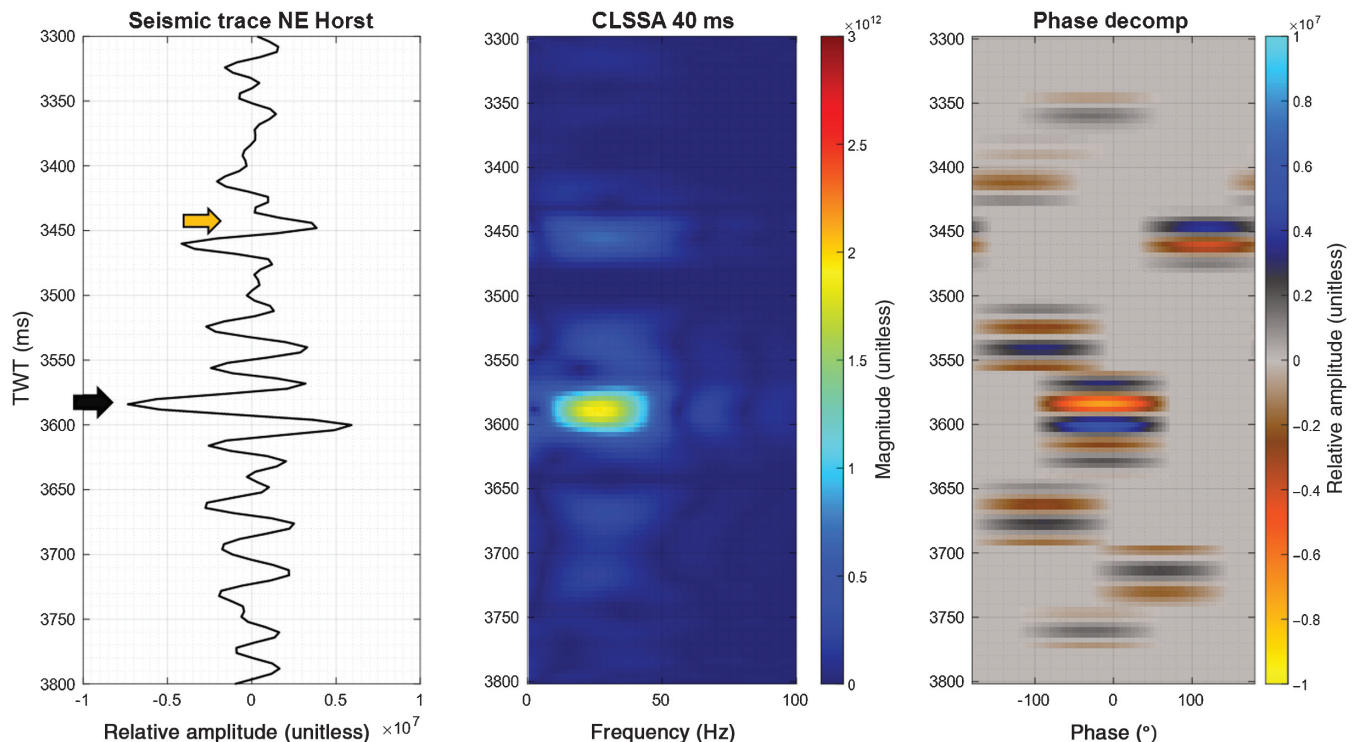


Figure 19. Time-variant spectral responses of a seismic located at the northeast horst: (a) seismic trace for the formation of interest (top of the main target marked with the black arrow, and the shallower semiregional event indicated with the black-orange arrow), (b) CLSSA time-frequency analysis, and (c) PD time-phase analysis.

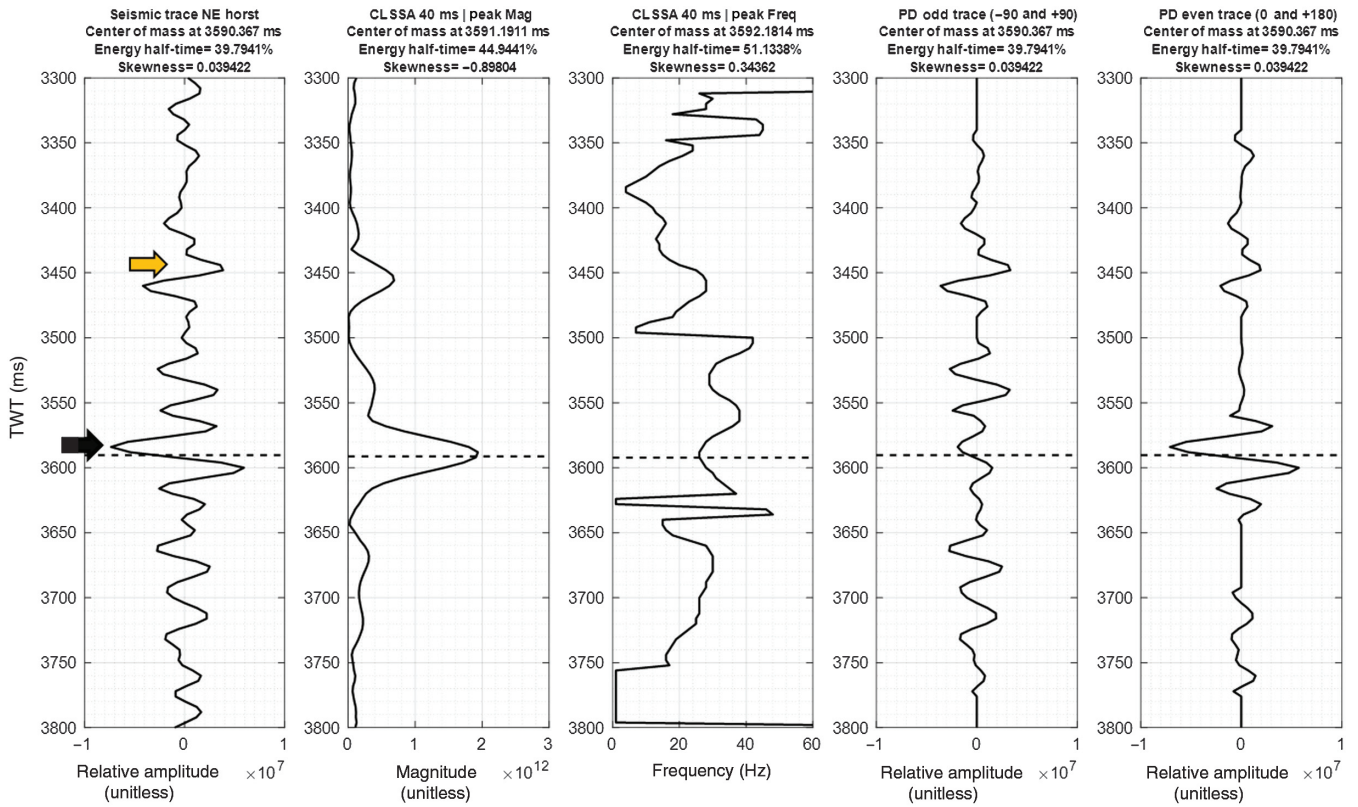


Figure 20. Time-variant spectral analyses attributes of a seismic trace at the northeast portion of the trap: (a) seismic trace for the formation of interest (top of the main target marked with the black arrow, shallower semiregional event indicated with the black-orange arrow), (b) CLSSA peak magnitude, (c) CLSSA peak frequency (Hz), (d) PD odd trace (-90° and $+90^\circ$), and (e) PD even trace (0° and 180°). On top of each track, there is the corresponding center of mass location, energy half-time, and skewness. Interval for metric calculation for all tracks is defined by the interpreted top and base events on the seismic trace on (a). Center of mass for each track is shown as a dashed line.

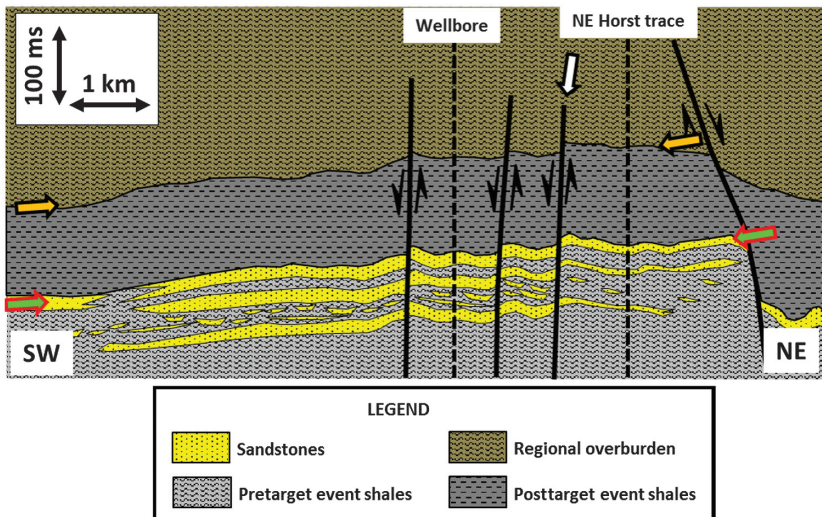


Figure 21. Southwest–northeast vertical section displaying the first-order schematic structural and stratigraphic interpretation based on the time-variant spectral analyses. The target horizon top event is indicated with the green-red arrow and tracked by the black horizon, and the shallower semiregional event is indicated with the black-orange arrow. The northwest–southeast fault under scope is indicated with a black-white arrow, whereas the wellbore-collocated and sample northeast horst sample traces are also indicated with black dashed lines. The line orientation is indicated in Figure 13.

This geologic scenario needs to be challenged by a detailed 3D interrogation of the input data set and its time-variant spectral attributes at several stratal levels within unbiased and sound structural, stratigraphic, and sedimentological frameworks, which was out of the scope of this paper.

Conclusion

This case study shows that the phase components that preferentially illuminate the target bed are not only dependent on the proximity of an interfering thin bed to the target bed but also on the assumed wavelet embedded on the seismic data. The inherent deficit of lower frequencies in the low end of the seismic bandwidth of the data set may be responsible for the long coda (several sidelobes) observed on the well-based extracted wavelet that we believe is more representative of the seismic data at target. This wavelet character is exacerbated when a derivative is taken, which translates to a longer

reach of mutual interference between thin beds, causing the preferential phase illumination at target to be sensitive to interfering thin beds that are located farther apart, at vertical separations in which an interpreter/analyst may think that no significant interference could occur.

The joint time-frequency and time-phase analysis performed on the field seismic data provides evidence that supports the interpretation hypothesis that some faults in this area may be syndepositional at a geologic time earlier than or around deposition of the target bed: In terms of time-frequency analysis, changes of peak frequency and peak magnitude across a particular secondary fault are consistent with the interpretation of larger amounts of sands being present in the downthrown side of the fault. Preferential phase illumination provides even more compelling evidence supporting this interpretation because preferred phase components sharply change across the fault. This change on the preferential illumination can be associated with changes on the interference patterns on both sides of the fault, which can be then used to qualitatively infer the relative amount of interfering layers on each block.

Acknowledgments

The authors wish to thank G. Haughey, M. Flores, C. Moreno, M. Silva, O. Portniaguine, Lumina Geophysical, and the University of Houston. Thanks to BHP and its partners for their support and permission to use and publish the proprietary data set.

Data and materials availability

Data associated with this research are confidential and cannot be released.

References

- Barnes, A. E., 2016, Handbook of poststack seismic attributes: SEG, Geophysical References Series 21.
- Bracewell, R. N., 2000, The Fourier transform and its applications: McGraw-Hill.
- Castagna, J. P., A. Oyem, O. N. Portniaguine, and U. Aikulola, 2016, Phase decomposition: Interpretation, **4**, no. 3, SN1–SN10, doi: [10.1190/INT-2015-0150.1](https://doi.org/10.1190/INT-2015-0150.1).
- Castagna, J. P., S. Sun, and R. W. Siegfried, 2003, Instantaneous spectral analysis: Detection of low-frequency shadows associated with hydrocarbons: The Leading Edge, **22**, 120–127, doi: [10.1190/1.1559038](https://doi.org/10.1190/1.1559038).
- Chakraborty, A., and D. Okaya, 1995, Frequency-time decomposition of seismic data using wavelet-based methods: Geophysics, **60**, 1906–1916, doi: [10.1190/1.1443922](https://doi.org/10.1190/1.1443922).
- Connolly, P. A., 1999, Elastic impedance: The Leading Edge, **18**, 438–452, doi: [10.1190/1.1438307](https://doi.org/10.1190/1.1438307).
- Meza, R. G., G. Haughey, J. P. Castagna, U. Barbato, and O. N. Portniaguine, 2016, Phase decomposition as a hydrocarbon indicator: A case study: 86th Annual International Meeting, SEG, Expanded Abstracts, 1839–1843.

- Meza, R. G., J. A. Sierra, J. P. Castagna, and U. Barbato, 2018, Joint time-variant spectral analysis — Part 1: Forward modeling the effects of thin-bed layering: Interpretation, **6**, this issue, doi: [10.1190/int-2018-0048.1](https://doi.org/10.1190/int-2018-0048.1).
- Okaya, D. A., 1995, Spectral properties of the earth's contribution to seismic resolution: Geophysics, **60**, 241–251, doi: [10.1190/1.1443752](https://doi.org/10.1190/1.1443752).
- Partyka, G., J. Gridley, and J. Lopez, 1999, Interpretational applications of spectral decomposition in reservoir characterization: The Leading Edge, **18**, 353–360, doi: [10.1190/1.1438295](https://doi.org/10.1190/1.1438295).
- Puryear, C. I., O. N. Portniaguine, C. M. Cobos, and J. P. Castagna, 2012, Constrained least-squares spectral analysis: Application to seismic data: Geophysics, **77**, no. 5, V143–V167, doi: [10.1190/geo2011-0210.1](https://doi.org/10.1190/geo2011-0210.1).
- White, R. E., and R. W. Simm, 2003, Tutorial- good practice in well ties: First Break, **21**, 75–83.
- Widess, M. B., 1973, How thin is a thin bed?: Geophysics, **38**, 1176–1180, doi: [10.1190/1.1440403](https://doi.org/10.1190/1.1440403).



Ramses Meza received a geophysical engineering degree from the Universidad Simon Bolivar (Venezuela), an M.S. in geophysics from the Colorado School of Mines (USA), and a Ph.D. in geophysics from the University of Houston. He is a principal geophysicist with BHP. Early in his career, he worked as a reservoir geophysicist at Petroleos de Venezuela S. A. (PDVSA) in Puerto La Cruz, Venezuela; Harvest-Vinccler in Maturin, Venezuela; and ConocoPhillips in Houston, Texas, USA. His responsibilities included support in terms of quantitative seismic interpretation for hydrocarbon exploration and production activities. Since 2012, he has been with BHP as a subject-matter expert providing advanced geophysical support to all E&P assets with emphasis on integration of quantitative interpretation (QI) products, visualization, seismic attributes, QI quality assurance, seismic reservoir characterization, DHI analysis, and risking. He is a member of SEG, AAPG, EAGE, and SOVG.



J. Antonio Sierra received a B.S. in geology and geophysics and an M.S. in geophysics from the University of Houston. Currently, he is an exploration geophysicist at EOG Resources focused on generating prospects in the Columbus Basin, offshore Trinidad and Tobago. In addition, he has designed and executed seismic acquisition and processing campaigns optimized for detailed structural and quantitative seismic interpretation. He was previously a geophysicist at BHP Billiton as part of their Rock and Fluid Physics team doing quantitative seismic interpretation for conventional and unconventional plays. While at BHP Billiton, he also worked in the seismic processing and imaging team with a focus on building seismic velocity models.



John P. Castagna received a B.S. (1976) in geology from Brooklyn College, a master's degree (1981) in high-temperature geochemistry, and a doctoral degree (1983) in exploration geophysics from the University of Texas at Austin. He currently holds the Robert Sheriff Chair of geophysics at the University of Houston. He

specializes in exploration geophysics research and development. He is widely known for his work in direct hydrocarbon detection and reservoir characterization. He joined ARCO's well logging research group in 1980. He served the company in several research, exploration, field development, and management positions. In 1982, he was named technical coordinator for Sonic Logging Research; in 1986, log analyst for Reservoir Engineering Services; in 1987, technical coordinator for Rock Physics Research; in 1988, director of Geoseismic Interpretation Research; and in 1989, manager of Seismic Analysis Research. In 1990, he transferred to Vastar Resources where he was responsible for development of an extension of major offshore Gulf of Mexico fields and exploration of surrounding acreage. He later joined ARCO International Oil and Gas Co., with responsibility for offshore China and Russia exploration. He returned to ARCO Research in 1995 and was assigned as visiting research scientist at the Geotechnology Research Institute of the Houston Advanced Research Center, where he was principal investigator for research projects funded by the Gas Research Institute, the Energy Research Clearing

House, and a consortium of energy companies. Also in 1995, he was named distinguished lecturer for SEG, delivering the fall lecture on "Applied AVO analysis: Use and abuse of amplitude variation with offset." He has served SEG in various other capacities including chairman of *The Leading Edge* editorial board, first vice-president, and technical program chairman for the 2003 Annual Convention in Dallas. His book, *Offset-dependent-reflectivity: Theory and practice of AVO analysis*, is an SEG bestseller. He has also served as associate editor for *GEOPHYSICS*. In 2000, he founded Fusion Geophysical, a geophysical contractor specializing in integrated seismic analysis. In February, 2010, he founded Lumina Geophysical, leading the industry in seismic spectral analysis, quantitative interpretation, and reservoir characterization. His main technical interest is quantitative seismic analysis in exploration and reservoir characterization.



Umberto Barbato received an M.S. in geophysics and seismology from the University of Houston. He is the manager of case studies at Lumina Geophysical; he has more than five years of experience working in the oil and energy industry. He is skilled in seismic interpretation, geophysics, earth science, and petroleum geology,

and he has several publications in spectrally based seismic attributes.